

SUPPORTING INFORMATION

NANOSTRUCTURE-SUPPORTED EVAPORATION UNDERNEATH A GROWING BUBBLE

*Shakerur Ridwan and Matthew McCarthy**

Department of Mechanical Engineering and Mechanics, Drexel University
3141 Chestnut St. Philadelphia, PA, 19104, USA

S1. Video Files

Video #1

Surface temperature distribution during ebullition cycles on a flat surface. Shown in real time.

Video #2

Local heat flux during ebullition cycles on a flat surface. Shown in real time.

Video #3

Local heat transfer coefficient during ebullition cycles on a flat surface. Shown in real time.

Video #4

Surface temperature distribution during ebullition cycles on a nanostructure coated surface. Shown in real time.

Video #5 Shown in real time.

Local heat flux during ebullition cycles on a nanostructure coated surface. Shown in real time.

Video #6

Local heat transfer coefficient during ebullition cycles on a nanostructure coated surface. Shown in real time.

Video #7

Local heat transfer coefficient during one extended ebullition cycle on a nanostructured surface, showing a nanostructure dry out event.

S2. Experimental apparatus

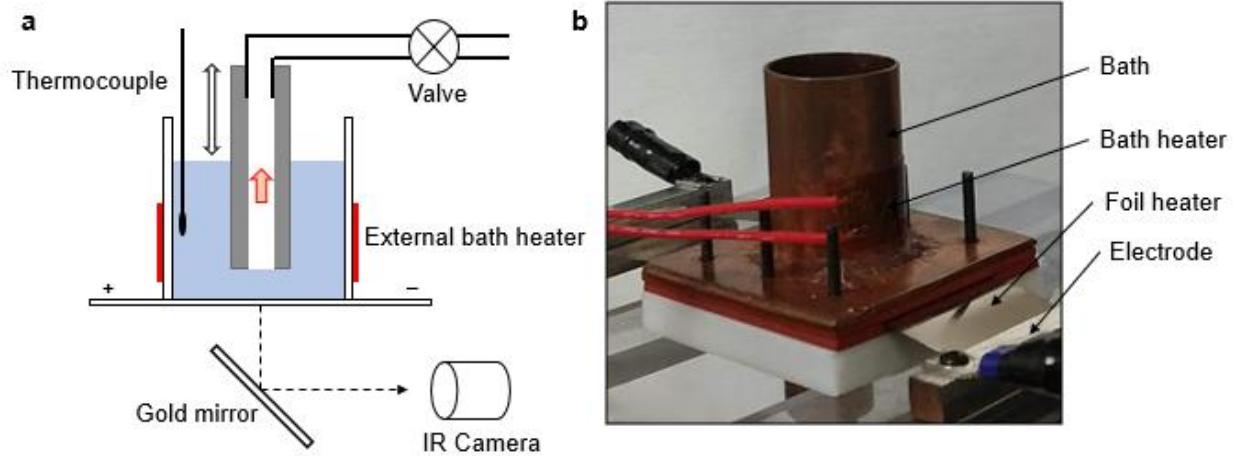


Figure S1. Experimental setup. (a) Schematic diagram of the experimental setup and, (b) Optical image of the setup

An image of the experimental set up is shown in figure S1. The main test chamber for water bath is 20mm diameter and 35mm high. An external flexible bath heater heats the bath to maintain saturation condition. Thermocouple inserted in the bath reads the bath temperature and connected with a programmable temperature controller. The bath heater is controlled by the controller to maintain required fluid temperature. A tube, inserted into the bath, is attached with a 3D micrometer. The movement of the tube can be precisely controlled by the micrometer. The outer diameter of the tube was 9.5mm, inner diameter was 3.18mm. A valve can control the vapor escape through the tube to atmosphere. The steel foil heater is electrically powered by a DC power supply Electro industries Model 4025. A gold mirror is placed at an angle of 45° with foil heater. A long wavelength IR camera FLIR A655SC was placed to receive radiation from the heater surface. The framerate of the IR camera used in the experiment was 25Hz, pixel size was $150\mu\text{m}$.

S3. Measurement technique and validation

S3.1 Infrared based measurement technique

An infrared thermal camera was used to view the backside of test surface and measure the temperature of the surface during experiment. In this experiment, A655-SC, a LWIR ($7\text{-}14\mu\text{m}$) camera was used for temperature measurement. The key measurement technique is to use an IR opaque element as a heater surface to prevent any kind of radiation emitted from the fluid atop the heater surface. The framerate used for the experiment was 25Hz. The framerate of the camera limits the experimental ability for research work, prevents boiling visualization using the IR camera. A blackbody BB703 was used for validation of IR camera temperature measurement. The opaqueness of heater surface ($25\mu\text{m}$ steel foil) was also tested with the blackbody.

S3.2 Emissivity and local temperature measurement

The emissivity of the steel foil changes with temperature. Hence, a spatial temperature variation of the surface, might not provide correct temperature data due change of emissivity with temperature. So, a black paint was sprayed at the backside of the steel foil, and emissivity of the paint was measured at different temperature. The emissivity of the black paint was measured experimentally using the setup shown in the figure S2. An aluminum plate was heated by a heater, and temperature of the aluminum plate was recorded by a thermocouple. High thermal conductivity of the aluminum (205 W/mK) ensured the uniform temperature of the aluminum block. The temperature of the black paint was recorded by the LWIR camera. Changing the heater power, aluminum block can be set at different temperature. Emissivity of the black paint was measured comparing the temperature obtained from the IR camera and thermocouple. The value of emissivity was independent of the temperature (0.89 ± 0.01).

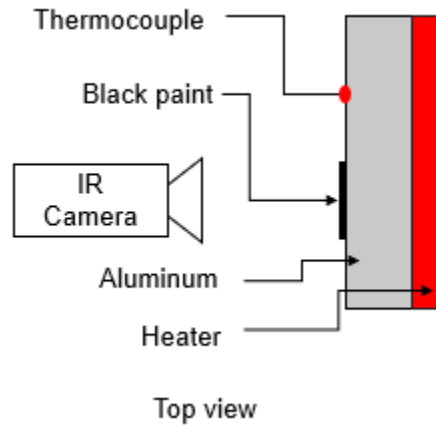


Figure S2. Schematics of the setup for emissivity measurement

S3.3 Local heat flux measurement:

Local heat transfer to the fluid was obtained by applying the conservation of energy to each pixel volume as shown in figure S3a. The size of the pixel was $150\mu\text{m}$, thickness of the foil was $25\mu\text{m}$. Lateral conduction due to temperature gradient within foil can be calculated using Fourier's law. Black paint at the backside has high emissivity (0.89 ± 0.01), which causes the radiative heat loss through the backside of the heating element. Additionally, convection to the air at the backside can cause convective loss. For measurement accuracy both convective and radiative loss was considered. Hence, energy balance for each pixel volume can be represented as follows:

$$q_f = q_g + q_{cond,in} - q_{cond,out} - q_{conv,loss} - q_{rad,loss} - q_{st} \quad (S1)$$

Considering all the losses and lateral conduction, the local heat flux supplied to the fluid can be calculated using the equation S2.

$$q'' = \frac{q_{fluid}}{\partial x^2} = \dot{q}_{electric}d + kd \left[\frac{\partial^2 T}{\partial x^2} + \frac{\partial^2 T}{\partial y^2} \right] - h_{air}(T - T_{\infty}) - \varepsilon\sigma(T^4 - T_{\infty}^4) - \rho Cd \frac{\partial T}{\partial t} \quad (S2)$$

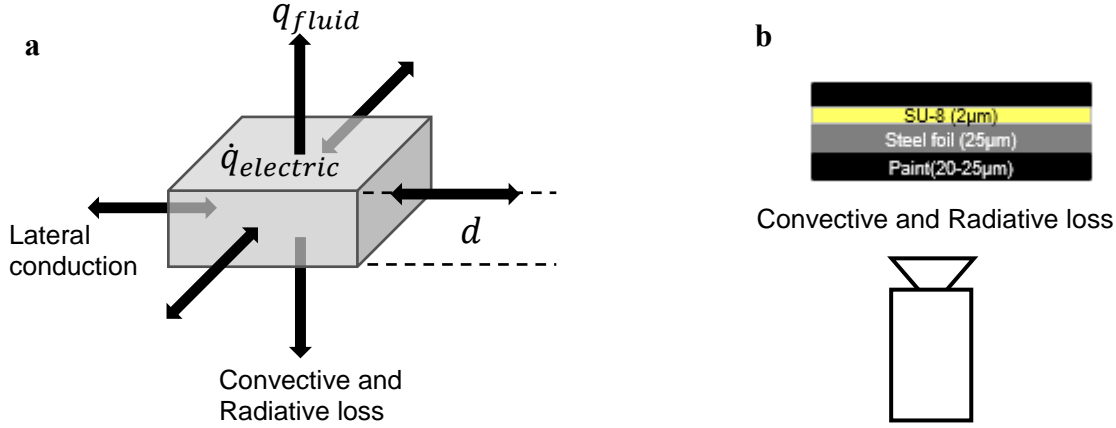


Figure S3. (a) Schematics of energy balance of each pixel volume, (b) Convective heat transfer of air measurement for backside heat loss

In the equation d represents the thickness of the heater surface. $T, T_{\infty}, \varepsilon, C$, represents the surface temperature, temperature of the air at the backside of the foil, emissivity of the surface/black paint, specific heat of the heater material, respectively. Density, specific heat, thermal conductivity of the steel foil was 8027.172 kg/m³, 490 J/kgK, 14 W/mK respectively. The equation says that, the local heat flux depends on four different parameters ($T, \dot{q}_{electric}, h_{air}, \varepsilon$). Local temperature of the foil was measured by IR camera, using the emissivity obtained experimentally for black paint. Volumetric heat generation rate due to Joule heating was calculated from the voltage drop measured and current applied to the foil ($\dot{q}_{electric} = \frac{VI}{Ad}$).

S3.4 Convective and radiative loss correction

Heat transfer coefficient of air to measure convective loss was measured experimentally. The steel foil was coated with black paint on both sides and heated electrically. Heat applied to the foil was transmitted to environment through radiation and convection. The emissivity value measured was used to find radiative heat transfer and was subtracted from total heat generation to evaluate convective heat transfer as well as heat transfer coefficient (11.5 W/m²K) due to natural convection. However, the existing correlation of Nusselt number can predict about the heat transfer coefficient of air (3% deviation from the experimental value). Hence, the correlation of Nusselt number and Rayleigh number was used to determine heat transfer coefficient for natural convection.

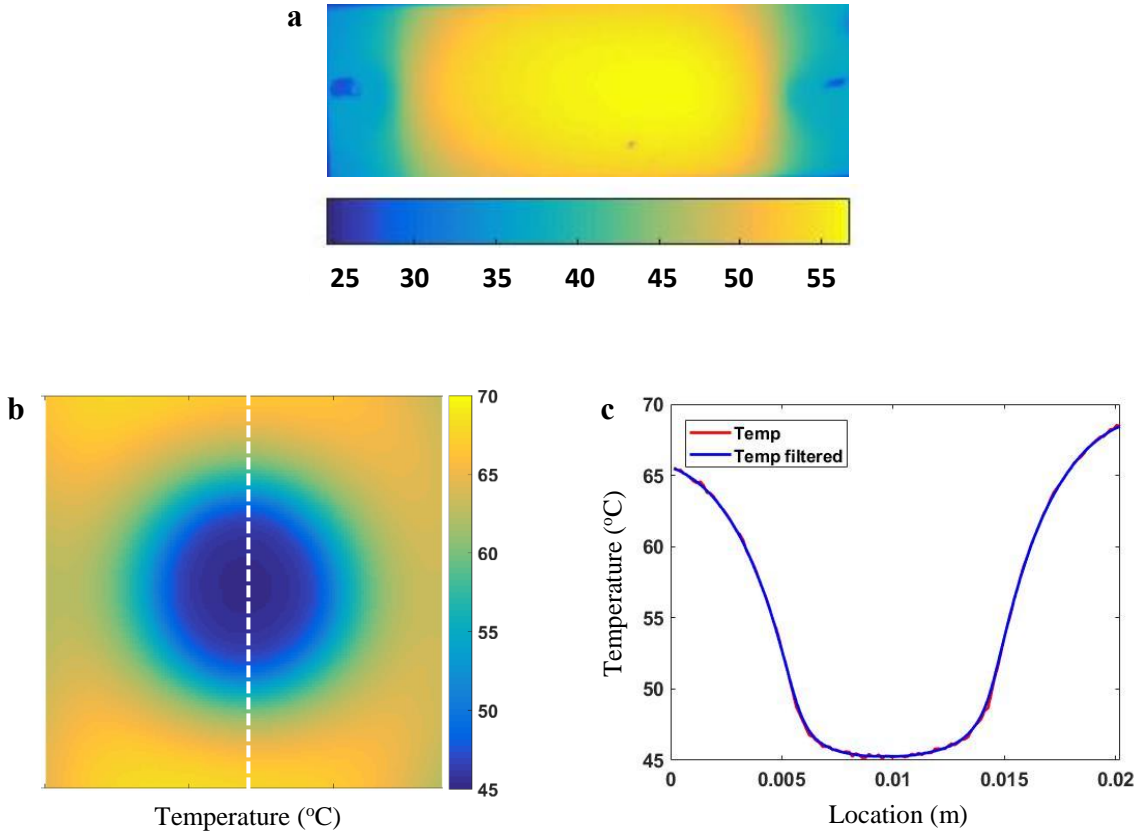


Figure S4. (a) Example of temperature distribution during the experiment for convective heat transfer coefficient of air, (b) Example of a 2D temperature distribution plot, (c) effect of low pass filter to remove noise of the temperature data

Temperature data recorded with IR camera was passed through low pass gaussian filter to remove the noise of temperature data. The effect of using filter is shown in the figure S4c.

S3.5 Lump capacitance validation

Although, we are using multiple layer of materials during experiments, no variation of temperature change along the thickness was assumed for local heat flux calculation. The assumption was validated experimentally. A 25 μ m steel foil heater was coated with 2 μ m SU8 layer, and black paint was sprayed on both sides of the foil as shown in figure S5. Gold mirrors were placed on both top and bottom of the surface. Heater was heated by applying electricity, and temperature data were collected from both top and bottom of the surface. To make a transient condition of the heating element, a nitrogen jet was applied suddenly atop the surface, and temperature data were collected at both top and bottom same point for the same spatial

location. The temporal plot of the temperature data shown in the figure S5b. The plot shows that, the temperature at the top and the bottom show no deviation from each other. This experiment ensures the thinness of the heater element for local heat flux calculation.

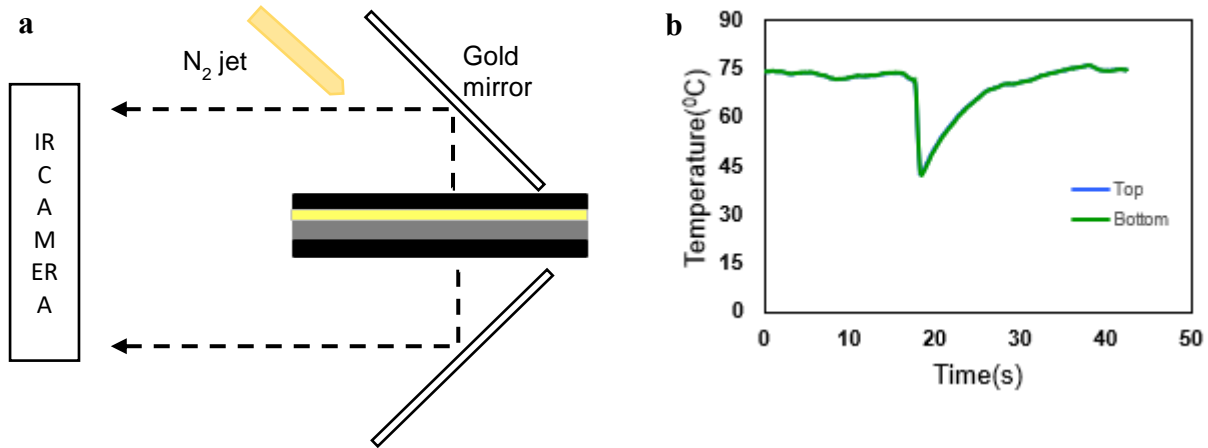


Figure S5. Thin film approximation. (a) Schematic of the experiment, b) experimental temperature data for the top and bottom at the same point f).

S3.6 Measurement validation

An experiment was conducted observing the heat flux supplied to the fluid using the experimental set up shown in the figure S6. The heater foil was heated by joule heating. A syringe pump infused water through a Teflon device. A thermocouple inserted can read the temperature of the water infused. The IR camera read the temperature of the heater. An optical camera was placed in the perpendicular direction to visualize the droplet/meniscus as shown in the figure S6a. A 3d micrometer can move the Teflon device in all three directions.

At first, a droplet is formed with the syringe pump. The device is moved vertically, so that the droplet touches the heater. The heater is turned on, and, the droplet is continuously fed water by the syringe pump at 3 μ L/min. Droplet turns into a meniscus and, start to recede. When the water evaporation rate from the meniscus counter balances the fluid supply rate to the meniscus, the meniscus becomes steady. IR camera reads the temperature data, and optical camera was used to see the size location of the meniscus. All the data were recorded, if the meniscus is steady at least for 2-3 minutes. The data were recorded for ~10s.

Based on the local heat flux data at steady state, the local heat flux data at the dry region observed validates the measurement accuracy. The plot shows that, the heat flux to the fluid, which is a mixture of air and vapor, and, the loss due to convection to air has a similar value (~500W/m²) as expected in the dry region. As air is residing at the upper surface of heated foil, a slightly higher average value of heat flux is observed than the convection to fluid at dry region, as expected from the correlation of Nusselt number. At the center region, heat transfer to fluid is

due to convection to water ($\sim 1200\text{W/m}^2$), which is higher than the convection loss to air. Water possesses higher heat transfer coefficient than air, and more heat is transferred to water due to convection. In between the two regions, a higher heat flux region, which represents the low resistance thin film region, was observed as shown in Figure S6c. Optical camera was used, to validate the location of different region and compare with the data from IR technique as shown in figure S6c. Location and size of the meniscus were experimentally determined and were correlated with the temperature and heat-flux distribution. High heat flux peak was observed at the vicinity of the 3-phase contact line.

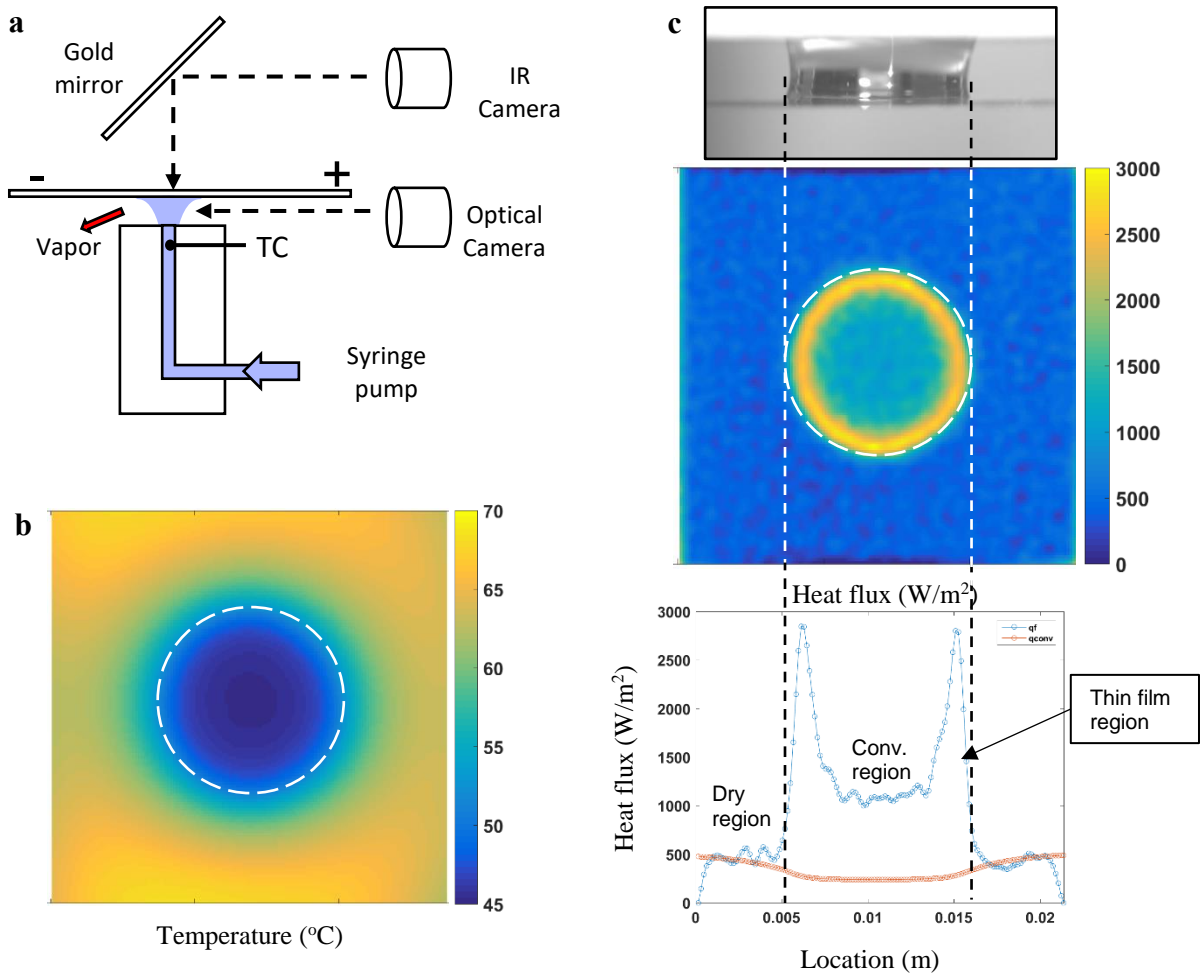


Figure S6. Experiment for measurement validation. (a) Schematic diagram of the experimental set up to form steady meniscus and visualize, (b) temperature distribution of the of the heated surface, (c) meniscus formed on a flat surface, heat flux distribution supplied to the fluid from the heated surface, heat flux distribution along the center line and determination of the heat transfer region.

S4. Nanostructure dry out analysis

S4.1 Dry out event prediction

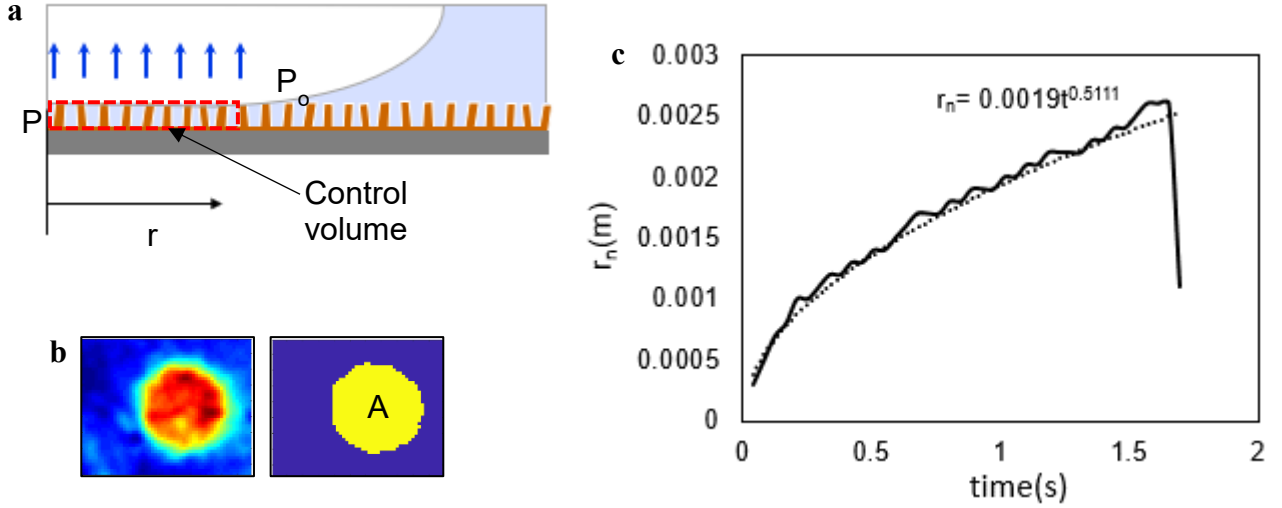


Figure S7. (a) Schematic showing the evaporation underneath a bubble, (b) schematic for the analysis of the liquid pressure measurement, measurement of nanostructure-supported 3phase region radius, (c) change of radius during bubble growth.

The viscous pressure drop through porous nanostructure due to liquid flow can be calculated using Darcy's law. However, the liquid velocity across the nanostructure deviates from the sink flow pattern due to evaporation across nanostructure-supported thin film region. When all the heat flux applied in the nanostructure-supported region was used for evaporation, the conservation of energy for any radial location in this region can be written as: $\dot{m}_{evap} = q''\pi r^2/h_{fg}$. While, for a control volume of any radial location, radially inward mass flow is $\dot{m}_{in} = -2\pi r V_r \rho_l$. As all the liquid entering the nanostructure supported region evaporates during bubble growth, then applying conservation of mass, the inward radial liquid velocity can be obtained by the equation:

$$V_r(t, r) = -\frac{\bar{q}''r(t)}{2\rho_l H h_{fg}} \quad (S3)$$

In this experiment, flow through the nanostructure is a transient process. The radius of the nanostructure-supported region is changing. For a radial flow, neglecting the diffusion and convective term, momentum equation can be written as:

$$\frac{dp}{dr}(r, t) = -\rho_l \frac{dV_r}{dt} \quad (S4)$$

As nanostructure is a densely structured thin porous medium, viscous effect for the bottom of the surface was negligible and avoided in the momentum equation. Viscous effect for the porous medium can be explained by the Darcy's law.

$$\frac{dp}{dr}(r) = \frac{\mu}{K} V_r \quad (\text{S5})$$

Negative sign was avoided as it was considered for velocity calculation of the inward radial flow. Incorporating Darcy's law with momentum equation, the pressure drop across the nanostructure-supported region can be calculated using these equations:

$$\frac{dp}{dr}(r, t) = \frac{\mu}{K} V_r - \rho_l \frac{dV_r}{dt} \quad (\text{S6})$$

$$P - P_o = \frac{dp}{dr} \Delta r \quad (\text{S7})$$

The permeability measurement technique of the nanostructure is demonstrated in the next section. The radius of the nanostructure-supported region was obtained using the experimental data by the equation: $r_n(t) = \sqrt{\frac{A(t)}{\pi}}$, as shown in the figure S7c. Where, A is the nanostructure-supported thin liquid film area. Average heat flux supplied to the fluid within the nanostructure-supported region can be calculated using the equation $\bar{q}'' = \frac{1}{A} \int q'' dA$.

Viscous pressure drop can provide the pressure in the liquid. The pressure difference between the liquid pressure and the pressure in the bubble can form a meniscus as shown in the figure S8a. The deflection of the liquid can change the height. Velocity, on the other hand, depends on the liquid film height. Hence, for each time step height is corrected for the pressure difference. Using an iterative approach for each time step pressure was calculated.

CuO nanostructure used in the experiment, is a randomly formed blade shaped structure. To simplify the analytical calculation and measurement, the structure can be represented as a cylindrical shaped structure. SEM images were analyzed to measure the roughness of the structured surface and gap between the structures, as explained in the permeability measurement section.

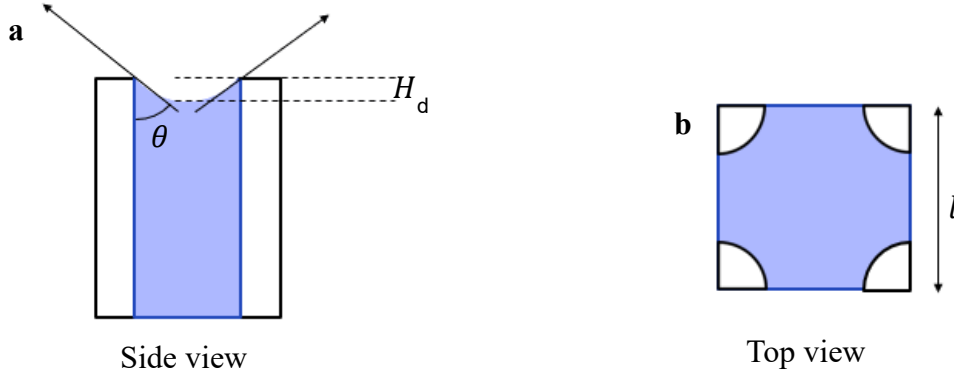


Figure S8. Schematic of a unit cell considered for force balance analysis at 3phase region, (a) side view and (b) top view

Applying the force balance, the capillary force due to structure equates the force due to pressure difference between the pressure within liquid and the pressure inside of the bubble. Hence,

$$\sigma_{lv} \cos \theta \pi D = (P - P_o) \left(l^2 - \frac{\pi}{4} D^2 \right) \quad (\text{S8})$$

The solid-liquid angle due to deflection can be calculated using the equation.

$$\theta = \cos^{-1} \left[\frac{P - P_o}{\pi D \sigma_{lv}} \left(l^2 - \frac{\pi}{4} D^2 \right) \right] \quad (\text{S9})$$

Angle measured from the previous equation can provide the height change due to deflection as shown in the figure S8a. Assuming the height of all the structures same, the curvature formed is a spherical cap. The deflected height along the diagonal of the unit cell was obtained using the equation:

$$H_d = (\sqrt{2}l - D) \frac{(1 - \sin \theta)}{2 \cos \theta} \quad (\text{S10})$$

Where, D was approximated as $D = 2l \sqrt{\frac{\phi}{\pi}}$. Average deflected height used for the calculation in the iterative process was, $H_{d,avg} = \frac{H_d}{2}$.

So, the height was corrected for each time step using the deflection height, and pressure difference of the liquid was calculated. This pressure difference was used in the next step of calculation for height.

S4.1 Permeability measurement of nanostructures

An experiment alike the section S3.6 was conducted with nanostructure to measure the permeability of the CuO nanostructure experimentally. A droplet, which touched the nanostructure coated surface, was formed. Initially, the surface was fully wet when the droplet touches the surface. For joule heating, the power through the foil is turned on, and meniscus starts to recede due to evaporation. The droplet/meniscus was continuously fed by the syringe pump at 3 μ L/min to make a steady meniscus. Apparent wet region on the nanostructured surface, was determined by the optical camera. IR camera recorded the temperature from the backside, as it was done for the flat surface.

The size of the meniscus, determined by the optical camera, on nanostructured surface (~1cm) was like the meniscus size on the flat surface as shown in figure S9. In case of nanostructure, the scenario looks different than that for the flat surface. A higher heat flux region was also observed for the nanostructure coated surface. In this case, the region was residing outside of the apparent wetted region. Nanostructure helps wicking, and maintains a thin nanostructured supported wet region, which possesses the higher heat flux region.

The data from the experiment was used to measure the permeability of the CuO nanostructure. Due to low thermal resistance at the nanostructure supported region, and, higher heat flux region to reside in the nanostructure supported region, it can be assumed that all the evaporation is taking place at this region. For a radial coordinate system, Darcy's law can be written as

$$dP = -\frac{\mu}{KA}\dot{V}_r dr, \quad A = 2\pi rH \quad (S11)$$

\dot{V}_r, r, H represent volumetric flow rate at the radial direction, radial location, and height of the nanostructure supported region respectively. K is the permeability of the porous nanostructure, and μ is the viscosity of the fluid. A uniform evaporation across the nanostructure supported region was assumed. Figure S9 displays the schematic of the modeling approach to measure permeability of the nanostructure. Here, r_1, r_2 represents the radius of the apparent wetted region and true wetted region respectively. Nanostructure supported evaporative region resides in between r_1 and r_2 . At $r = r_1$, $\dot{V}_t = \dot{V}_r$. At the region $r_1 < r < r_2$, $\dot{V}_t = \dot{V}_e + \dot{V}_r$. At $r = r_2$, $\dot{V}_r = 0$. Considering a small element dr near $r = r_1$,

$$\frac{\dot{V}_e}{\pi(r^2 - r_1^2)} = \frac{\dot{V}_t}{\pi(r_2^2 - r_1^2)} \quad (S12)$$

Hence, using the correlation between the volumetric flow rates, the radial volumetric flow rate can be obtained, where the volumetric flow rate infused from syringe pump (\dot{V}_t) is known.

$$\dot{V}_r = \dot{V}_t \left[1 - \frac{(r^2 - r_1^2)}{(r_2^2 - r_1^2)} \right] \quad (\text{S13})$$

Incorporating radial volumetric flow rate in the Darcy's law for porous medium, and, integrating for the region between $r = r_1$ and $r = r_2$, the equation to find the permeability of the nanostructure can be derived.

$$K = -\frac{\mu}{2\pi H \Delta P} \dot{V}_t \left[\ln\left(\frac{r_2}{r_1}\right) \left(1 + \frac{r_1^2}{r_2^2 - r_1^2}\right) - \frac{1}{2} \right] \quad (\text{S14})$$

Where, ΔP is the viscous pressure drop across the porous nanostructure. The flow through the nanostructure is driven by the capillary pressure. Capillary pressure at the end of the true wetted region for a receding meniscus, can be equated with the viscous pressure drop. An effective capillary pressure can be estimated using $P_c = -\frac{\Delta E}{\Delta V}$. Using the equation of Laplace pressure, and applying to the equation of Helmholtz free energy capillary pressure can be calculated.

$$\Delta P = P_c = -\frac{\sigma_{lv}}{\chi H} [(r_g - \phi)\cos\theta - (1 - \phi)] \quad (\text{S15})$$

Where χ, r_g, ϕ are porosity, roughness factor and solid fraction respectively. The relationship among the roughness, porosity and solid fraction can be derived as follows:

$$\chi = \frac{(r_g - 1)gap}{2H}, \quad \phi = 1 - \chi \quad (\text{S16})$$

Here, gap represents the void space within the blade shaped CuO nanostructure. Roughness factor (6.5) and gap (300nm) were obtained analyzing the SEM images of the nanostructure. Intrinsic contact angle of the CuO nanostructure is difficult to measure as after oxidation chemical process the oxide form as a nanostructure. Dubal *et al.* (2010)¹ measured the contact angle on copper oxide surface, formed by chemical bath deposition, reported as 53° contact angle. Meier *et al.* (1995)² used sessile droplet method to measure the contact angle of copper oxide-copper alloy. An addition of 1.5-10wt% of CuO was made. A minimum value of 42±8° contact angle was reported. However, in both cases the surfaces were not mirror finished to be considered as an intrinsic contact angle. The roughness of the surface reduces the apparent contact angle of the surface. In our calculation, the value of intrinsic contact angle was assumed to be 55°. However, the value permeability is less contingent on the contact angle. The nanostructure was found 91.7% porous, and permeability of the nanostructure estimated was ~5.38x10⁻¹⁵m². Based on the experimental work form Klinkenberg (1941)³, liquid permeability is a geometric property of the structure, and independent of mean applied pressure, liquid composition. The gas permeability measured by Lysenko *et al.* (2004)⁴ for porous Si

nanostructures was 10^{-16} to 10^{-15}m^2 , corresponding to the 50-70% porosity. Permeability was found to increase with porosity, and for liquid the value should be lower. Hence, measured/estimated permeability for the CuO nanostructure was in good agreement with the previous experimental measurement.

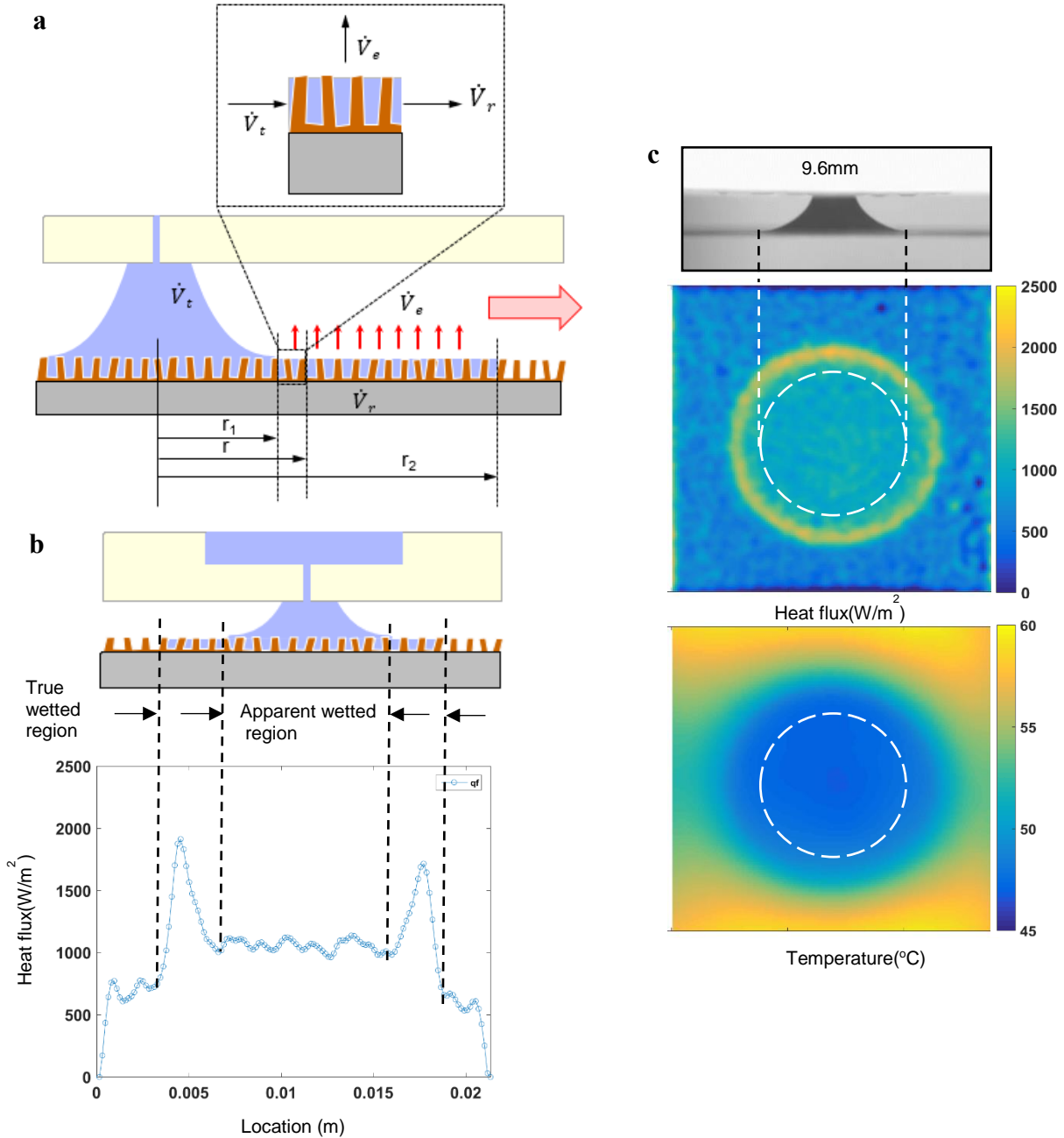


Figure S9. Experiment for permeability measurement. (a) Schematics for analytical analysis of permeability measurement for nanostructure, (b) determination of heat transfer region for the experiment with nanostructure, (c) meniscus formed on a nanostructure coated surface, heat flux distribution supplied to the fluid from the heated surface, temperature distribution of the heated surface.

S4.2 Experimental data of pressure profile and contact angle at different radial location

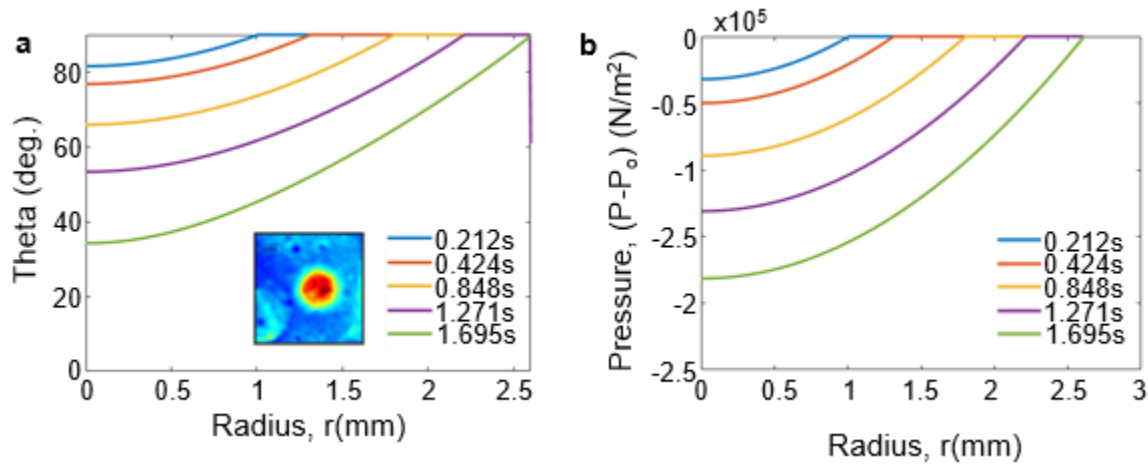


Figure S10. Calculation of liquid pressure for no dry out experiment. (a) Plot of the solid liquid angle formed at different radial location, (b) plot of pressure difference between the pressure in liquid and bubble obtained from the iterative calculation using experimental data.

The plot in figure S10b shows the pressure difference at different radial location underneath a bubble at different time. It shows that, as the time goes up, the radius of the nanostructure-supported 3phase region increases and the pressure difference at the center of a bubble gets lower. The curves show the change of pressure within the nanostructure-supported thin liquid film. Solid-liquid contact angle decreases up to $\sim 35^\circ$.

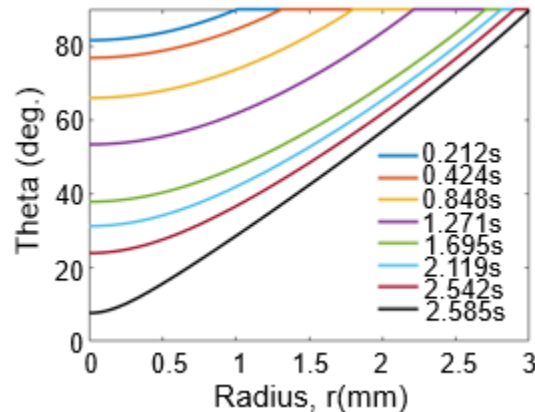


Figure S11. Validation of prediction for dry out event. (a) Plot of the angle formed at different radial location obtained from the analytical iterative calculation for the experiment of dry out event observed.

The nanostructure supported liquid film can deflect due to pressure difference. Dry out process starts when the solid liquid contact angle reaches the receding contact angle. In other way, thin liquid film region will start to dry out when the capillary pressure becomes scanty to overcome viscous pressure drop. The exact value for receding contact angle for CuO is not

known. Horsthemke *et al.*⁵ showed that receding contact angle of copper can vary within a range of 15°-45°. A smooth CuO deposition using highly reactive H₂O₂ solution showed a contact angle of 10°, which turned into 20° within several minutes⁶. The receding contact angle of the nanostructure material can be approximately as low as ~10° -20°. Moreover, capillary pressure is still enough (-198kPa) to overcome viscous pressure drop and maintain a thin liquid film within the nanostructure.

Figure S11 shows the plot of contact angle at different location and time. The plot shows that, the contact angle reaches as low as around 10° at around 2.6s. So, the analysis predicts that the dry out process should begin at around 2.6s.

References:

1. Dubal, D.; Dhawale, D.; Salunkhe, R.; Jamdade, V.; Lokhande, C., Fabrication of copper oxide multilayer nanosheets for supercapacitor application. *Journal of Alloys and Compounds* **2010**, *492* (1-2), 26-30.
2. Meier, A.; Chidambaram, P.; Edwards, G., A comparison of the wettability of copper-copper oxide and silver-copper oxide on polycrystalline alumina. *Journal of Materials Science* **1995**, *30* (19), 4781-4786.
3. Klinkenberg, L. In *The permeability of porous media to liquids and gases*, Drilling and production practice, American Petroleum Institute: 1941.
4. Lysenko, V.; Vitiello, J.; Remaki, B.; Barbier, D., Gas permeability of porous silicon nanostructures. *Physical Review E* **2004**, *70* (1), 017301.
5. Horsthemke, A.; Schröder, J. J., The wettability of industrial surfaces: contact angle measurements and thermodynamic analysis. *Chemical Engineering and Processing: Process Intensification* **1985**, *19* (5), 277-285.
6. Tu, S.-H.; Wu, H.-C.; Wu, C.-J.; Cheng, S.-L.; Sheng, Y.-J.; Tsao, H.-K., Growing hydrophobicity on a smooth copper oxide thin film at room temperature and reversible wettability transition. *Applied Surface Science* **2014**, *316*, 88-92.